Swift Observations of TANAMI Sources

Bachelorarbeit

vorgelegt von
Martina W. Müller

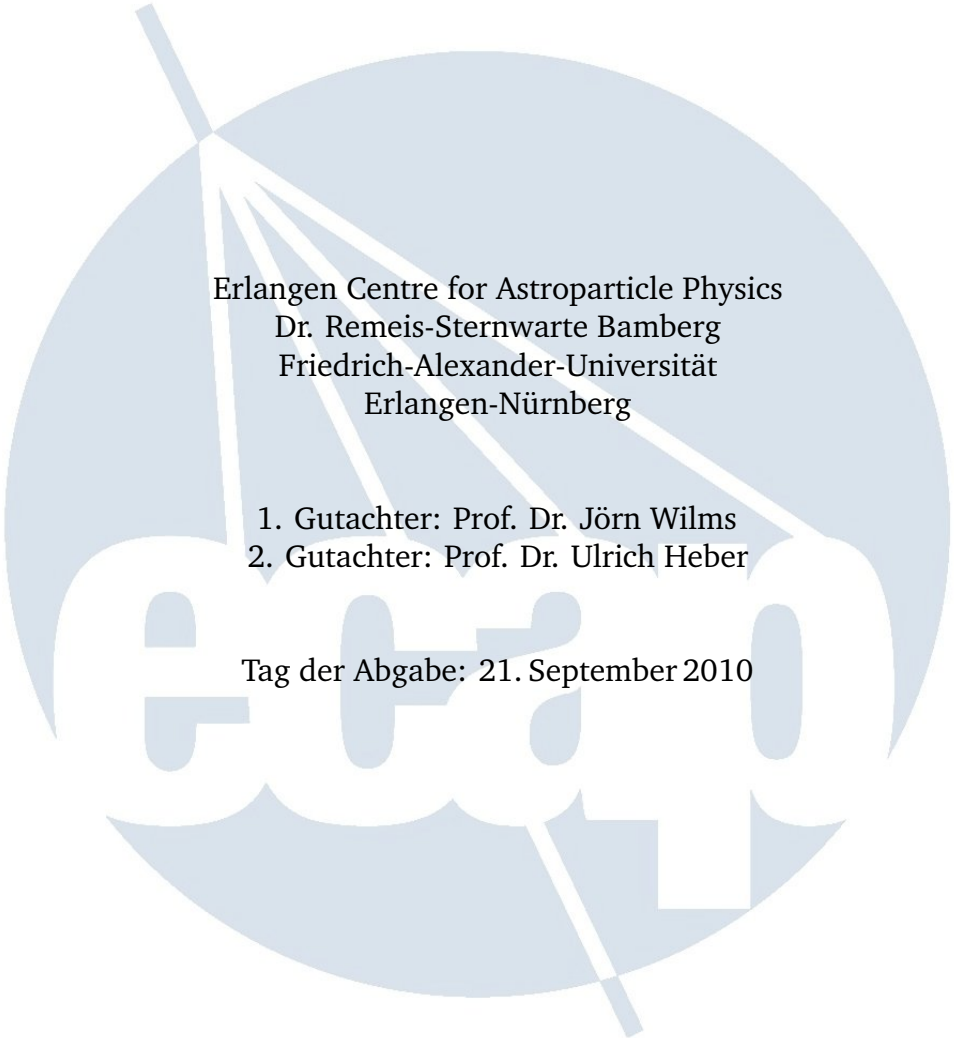

Erlangen Centre for Astroparticle Physics
Dr. Remeis-Sternwarte Bamberg
Friedrich-Alexander-Universität
Erlangen-Nürnberg

1. Gutachter: Prof. Dr. Jörn Wilms
2. Gutachter: Prof. Dr. Ulrich Heber

Tag der Abgabe: 21. September 2010

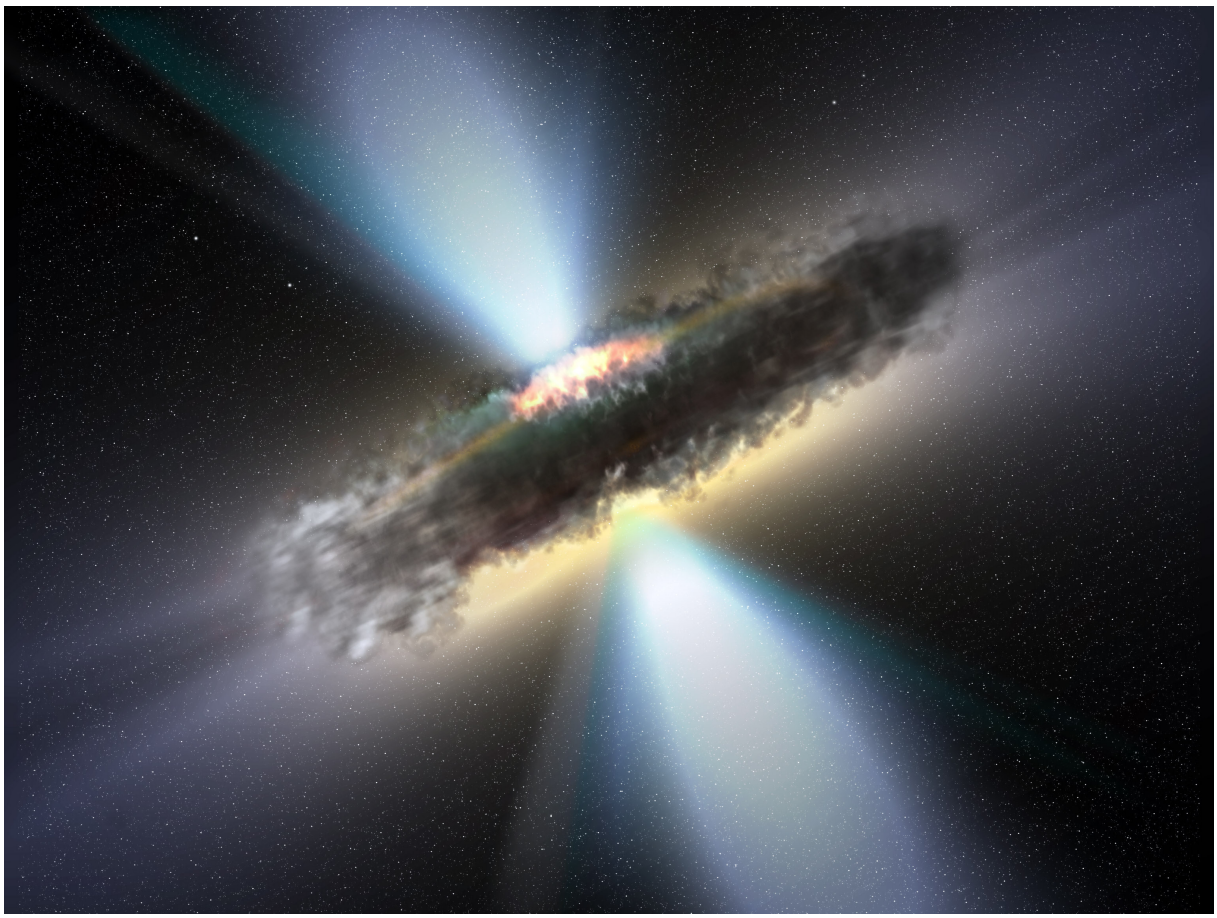

Figure 1: AGN obscured by dust torus (Credit: ESA / V. Beckmann, NASA-GSFC)

Abstract

Astronomy makes use of more than twenty decades of the electromagnetic spectrum, ranking from radio to gamma-rays. For observations of AGN (active galactic nuclei) in general and blazars in particular, X-ray observations are of great interest. This bachelor thesis presents X-ray observations of sources from the TANAMI sample. The sources were selected by the TANAMI program for VLBI-monitoring of AGN jets in the radio and were observed by the X-ray telescope of NASA's *Swift* satellite.

Thirteen out of twenty-six target sources were detected as strong sources. For these, spectra were extracted and a simple photoabsorbed power-law model was fitted. An additional absorption component was taken into account for those sources showing partial coverers. In addition, a broadband SED (spectral energy distribution) was compiled for PKS 2155−304, which includes additional data from *Swift*/UVOT, *Fermi*/LAT and the 100 m Effelsberg radio telescope.

Object of this thesis is the discussion of the obtained fit parameters as well as a statistical comparison of the sample with a supplementary source sample analyzed by Krauß (2010). As a main result, the two samples are found to be originating from the same source distribution with a probability of $\approx 75\,\%$.

Contents

1 Introduction **1**
- 1.1 AGN . . . 1
  - 1.1.1 Power generation in AGN . . . 1
  - 1.1.2 Taxonomy and unified model . . . 2
- 1.2 Blazars . . . 4
  - 1.2.1 Jets models and blazar spectra . . . 4
  - 1.2.2 Unification scheme . . . 5
- 1.3 The TANAMI project . . . 6

2 Data **8**
- 2.1 *Swift* . . . 8
- 2.2 XRT . . . 9
- 2.3 Sample selection . . . 11
- 2.4 Data reduction . . . 11
- 2.5 Data analysis . . . 11

3 Observations **15**
- 3.1 Strong sources . . . 15
- 3.2 Weak sources . . . 31
- 3.3 Not detected sources . . . 32
- 3.4 USNOA2 0525−42507178 . . . 33

4 Results **34**
- 4.1 Photon indices . . . 34
- 4.2 Absorption coefficients . . . 35
- 4.3 AGN statistics . . . 36

5 Summary and outlook **38**

Chapter 1

Introduction

1.1 AGN

Active Galactic Nuclei (AGN) are a class of astrophysical objects including BL Lac-objects, quasi stellar objects (QSOs), Seyfert-galaxies and radio galaxies. They are characterized by very high luminosities throughout the electromagnetic spectrum. AGN exhibit nonthermal spectra. For frequency ν and flux density F_ν, the observed νF_ν spectra are generally flat, which implies similar emission per frequency decade. In addition, most AGN show strong variability on timescales from days to years (e.g., Krolik, 1999).
The prevalent theory describes AGN as complex models. The central component of the standard model is a supermassive black hole, with a typical mass of the order of 10^6 to 10^8 solar masses. The very high observed luminosities on the scale of $\approx 10^{10}$ solar luminosities, a value comparable to the luminosity of whole galaxies, are believed to be caused by accretion of matter onto the black hole (Wilms & Kadler, 2010). A more detailed description of the AGN standard model is given in subsection 1.1.2. Many questions concerning AGN still are unanswered and will remain subject to future research.

1.1.1 Power generation in AGN

As AGN exhibit very high luminosities, it is important to understand the process they are powered by. The prevailing theory is that the radiated energy is gained from gravitational energy of material being accreted from an accretion disk onto the central black hole. A comparison (as in Wilms & Kadler, 2010) of accretion to nuclear fusion – the main energy source in stars – shows the high efficiency of this process.
With a proton mass of m_p and a Helium mass of m_He, the energy produced per proton in a $4\,\mathrm{H} \longrightarrow \mathrm{He}$ reaction is characterized by the efficiency η as follows:

$$\Delta E_\mathrm{nuc} = \frac{(m_\mathrm{He} - 4m_\mathrm{p}) \cdot c^2}{4} = \eta_\mathrm{nuc} \cdot m_\mathrm{p} c^2 \tag{1.1}$$

c is the speed of light in vacuum. The calculated efficiency is $\eta_\mathrm{nuc} = 0.007$. This is equivalent to a liberated energy of $\approx 6 \cdot 10^{18}\,\mathrm{erg\ g^{-1}}$.
For accretion, the efficiency can be computated from the accreted energy per particle

$$\Delta E_\mathrm{acc} = \frac{GMm}{R_\mathrm{S}} = \eta_\mathrm{acc} \cdot m c^2 \tag{1.2}$$

where G is the gravitational constant, M is the mass of the black hole, m is the mass of the accreted particle, and $R_\mathrm{S} = 2GM/c^2$ is the Schwarzschild-radius of the black hole. This

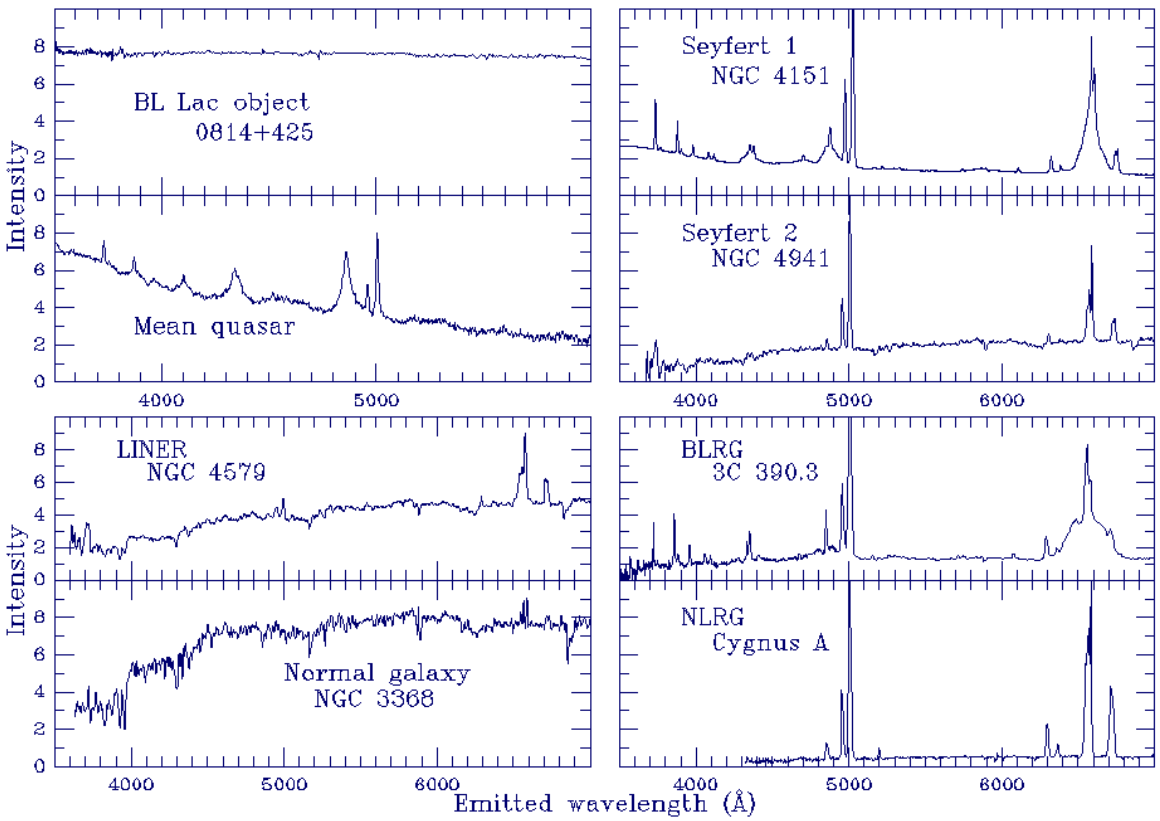

Figure 1.1: Optical AGN spectra (Credit: Keel, 2002)

corresponds to an efficiency of $\eta_{\mathrm{acc}} = 0.1$, which equates to a liberated energy of $\approx 10^{20}\,\mathrm{erg\ g^{-1}}$. This means that an accretion rate of $1...2\,\mathrm{M_\odot/yr}$ is sufficient to explain the observed typical AGN luminosities of $L \approx 10^{10} L_\odot$.
Accretion thus is the most efficient astrophysical energy source (Wilms & Kadler, 2010). However, this process can only take place as long as the radiation pressure does not exceed the gravitational force. This constraint is described by the Eddington limit L_{Edd}, which is an upper limit for the luminosity of the black hole

$$L < L_{\mathrm{Edd}} = \frac{4\pi GMmc}{\sigma_{\mathrm{T}}} = 1.3 \cdot 10^{38}\,\mathrm{erg\ s^{-1}} \cdot \frac{M}{M_\odot} \tag{1.3}$$

where σ_{T} is the Thompson cross-section. The luminosity as well can be described by the accretion efficiency as $L = \eta_{\mathrm{acc}} \cdot \dot{M} c^2$, which yields an upper limit for the accretion rate $\dot{M}$ of:

$$\dot{M}_{\mathrm{max}} = \frac{L_{\mathrm{Edd}}}{\eta_{\mathrm{acc}}\, c^2} \tag{1.4}$$

1.1.2 Taxonomy and unified model

AGN taxonomy is based on the source spectra. Typical optical AGN spectra can be seen in Fig. 1.1. The observed continua are described well by power-law functions $F_\nu \propto \nu^{-\alpha}$ which defines the photon index as $\Gamma = \alpha + 1$. Mainly two types of AGN can be distinguished from the optical spectra: Type 1 AGN feature broad (FWHM up to $10^4\,\mathrm{km\ s^{-1}}$) allowed emission lines as well as narrow (FWHM of a few $10^2\,\mathrm{km\ s^{-1}}$) emission lines of forbidden transitions while Type 2 AGN exhibit only narrow forbidden lines (Wilms & Kadler, 2010).
These and other observations have led to the development of a unified model for AGN, which is presented schematically (not to scale) in Fig. 1.2. This current paradigm states, that all AGN are intrinsically the same phenomenon at different luminosities and observed

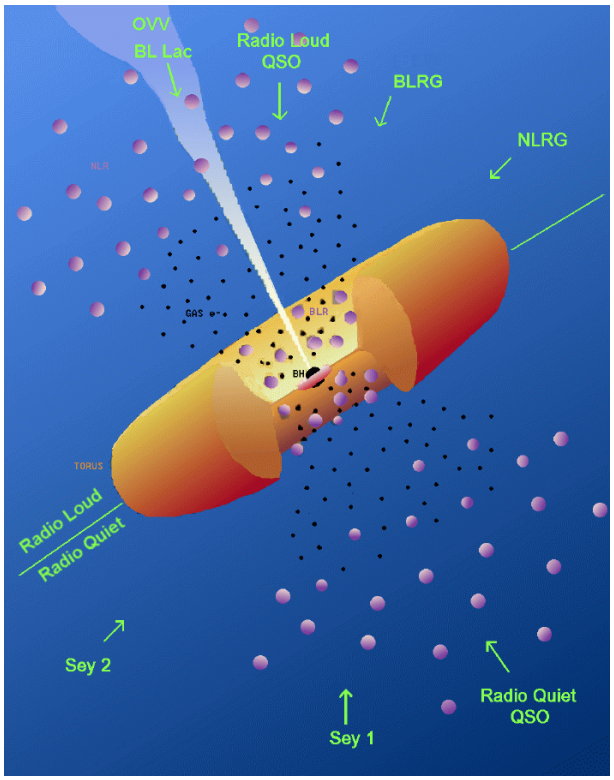

Figure 1.2: Scheme of the unified model
Credit: C. M. Urry and P. Padovani (1995)

under different viewing angles. The model describes the major components: A central black hole is surrounded by a luminous accretion disk and an obscuring dust torus. Optical emission lines are produced in clouds orbiting above the accretion disk. Narrow lines are believed to originate from transitions in the narrow line region (NLR), a low density medium ($n \approx 10^3 \cdots 10^6\,\mathrm{cm}^{-3}$) extending approximately from 100 to 1000 pc. The broad lines in type 1 AGN are generated in the broad line region (BLR), a dense medium ($n \approx 10^{10}\,\mathrm{cm}^{-3}$) with high velocities ($v \approx 1000 \cdots 5000\,\mathrm{km\ s}^{-1}$) which is located close to the black hole at distances of approximately 0.01 to 0.1 pc. For type 2 AGN, the BLR is not visible, as the AGN's center is obscured, particularly at optical and ultraviolet wavelengths, by the torus due to the line of sight.

The second important criterion in AGN taxonomy is the radio luminosity. Radio-loud AGN feature relativistic jets, emanating from the nucleus at relativistic speeds, which emit from radio through gamma-ray wavebands. The radio emission of these jets is believed to be synchrotron radiation emitted by relativistic jet particles. As these jets are absent in radio-quiet AGN, their radio luminosity is considerably lower. Radio jets have been detected on scales from 10^{17} to several 10^{24} cm, which makes them a factor of ten larger than the largest known galaxies (Urry & Padovani, 1995).

In summary: the unified model describes AGN as one class of similar galactic nuclei, from which the different source types can be distinguished by angle of view and luminosity. All major source types are shown in Fig. 1.2. Seyfert 2 galaxies are radio-quiet type 2 AGN, which means an edge-on view, while Seyfert 1 galaxies are type 1 AGN, that is they are seen face-on. Radio-quiet QSOs are a more luminous version of Seyferts. Low-ionization nuclear emission line region galaxies (LINERs, not in the figure) can be distinguished from Seyfert 2 galaxies by their weaker continuum.

Broad line radio galaxies (BLRGs) and narrow line radio galaxies (NLRGs) are the radio-loud counterpart to Seyferts type 1 and 2, respectively, while radio-loud QSOs, also known as quasi-stellar radio sources (Quasars), correspond to radio-quiet QSOs. In addition, jet sources

Figure 1.3: Blazar sequence (Donato et al., 2001, based on Fossati et al., 1998)

can be seen with the jet pointing directly at the observer: this model accounts for the blazar class, which includes BL Lac objects (named after their prototype BL Lacertae) and optically violent variable quasars (OVV quasars) as well as flat spectrum radio quasars (FSRQs).

1.2 Blazars

Among AGN, blazars represent the most powerful sources. Blazars are characterized by a beamed continuum, which is due to plasma moving relativistically in the jet, along the line of sight, as well as extreme variability on time scales as short as hours. The name blazar was brought up in 1978 by Edward Spiegel as an umbrella term combining BL Lacs and OVV quasars, emphasizing their "blazing" nature. Current taxonomy also includes FSRQs. These are objects similar to BL Lac objects in their continuum but with superposed emission lines of significant equivalent widths (EW). BL Lacs show only very narrow emission lines of EW $\lesssim 5$ Å.

1.2.1 Jets models and blazar spectra

Blazar spectra are nonthermal, as they are dominated by broadband jet emission. Currently, two different models are debated for the composition of blazar jets. Leptonic models suggest that the jet plasma consists of electron-positron pairs, while hadronic models consider electron-proton jets. The two approaches supply fundamentally different explanations for the acceleration of these jet particles to relativistic energies and, in consequence, for the observed blazar spectra.
Although blazars were first detected in the optical and radio, a large part of their emitted energy is at high energies. A series of typical averaged blazar spectra, the so-called "blazar sequence" (Fossati et al., 1998), can be seen in Fig. 1.3. For each spectra, the two dominant components can be seen as the two major humps in the νF_ν-spectra. Both leptonic and hadronic models agree that radio emission from jets is primarily due to synchrotron radiation of accelerated jet particles. One can assume a power-law electron distribution $\propto E^{-p}$,

which in return yields a power-law spectrum. Synchrotron self-absorption plays a role in the low-frequency part of the spectrum, as synchrotron emitting electrons can as well absorb soft synchrotron photons. This produces an overall spectral shape of

$$P_\nu \propto \nu^{\frac{5}{2}} \qquad \text{for low } \nu \tag{1.5}$$

$$P_\nu \propto \nu^{-\frac{(p-1)}{2}} \qquad \text{for high } \nu \tag{1.6}$$

with P_ν being the emitted power density at frequency ν.
The two jet models do not, however, concur in their explanations of the higher energetic spectral components. Leptonic models for jets interpret the second hump to be caused by inverse-Compton upscattering of seed photons. Target electrons are the same electron population producing the synchrotron component. The energy gained in this process depends on the Lorentz factor γ of the jet particles as $E_{\text{upscattered}} = \gamma^2 \cdot E_0$. As seed photons, both the synchrotron photons themselves (SSC = synchrotron self Compton-models) and an external radiation field (EC = external radiation Compton-models) come into question. Sikora, Begelman & Rees (1994) have shown observational evidence that strongly favors EC models over SSC models.
As an alternative to leptonic models, hadronic models posit the high-energy spectral components to be produced in reactions involving high-energy protons, e.g., in hadron-hadron or photon-hadron collisions or in pair production, and the resulting e^+e^--cascades. However, these models cannot fully explain the observed blazar X-ray spectra (e.g., Wilms & Kadler, 2010).

The observed average spectral energy distributions (SEDs) show a remarkable continuity seen in three systematic trends: First of all, the first peak occurs in different frequency ranges with more luminous sources peaking at lower frequencies. Secondly, the peak frequencies of the two humps are correlated. Finally, the luminosity ratio between the two peaks increases with bolometric luminosity. This supports the thesis that the blazar overall SED can be parameterized on the basis of only one parameter related to luminosity (Donato et al., 2001). For observing blazars, the X-ray band is especially important. Figure 1.3 shows that fluxes in this frequency range are rather low, as the X-ray observes the part of the spectra lying in the valley between the two peaks. Depending on the peak frequencies, both rising and falling slopes are to be expected. For high-frequency peaked sources, observations will see a dominating synchrotron component, which corresponds to falling slopes and thus photon indices of $\Gamma < 2$. This is implied by the broadband component of $N_{ph} \propto E^{-\Gamma}$, which yields a spectral shape of $F_\nu \propto E^{1-\Gamma}$ and consequently $\nu F_\nu \propto E^{2-\Gamma}$. On the other hand, observations of low-frequency peaked sources will see an excerpt of the spectra in which the inverse Compton component dominates, and will therefore yield photon indices of $\Gamma > 2$. Sources with approximately flat spectrum in the X-ray, that is with $\Gamma \approx 2$, are rather unlikely to be observed, as this means the observation of the flux minimum between the two humps. Another major reason for the deficiency of observed flat spectrum sources is that the flat part of the spectrum is a rather small frequency band compared to the broad frequency ranges of rising and falling spectral slopes, respectively.

1.2.2 Unification scheme

As we can see, distinction between different sub-classes of BL Lacs, corresponding to differences in the overall SEDs, has proved to be difficult due to a certain continuity in the spectral properties. For this reason, a unifying scheme was proposed by Ghisellini et al. (1998), showing a possible connection between BL Lacs and FSRQs. This unified view of blazars states

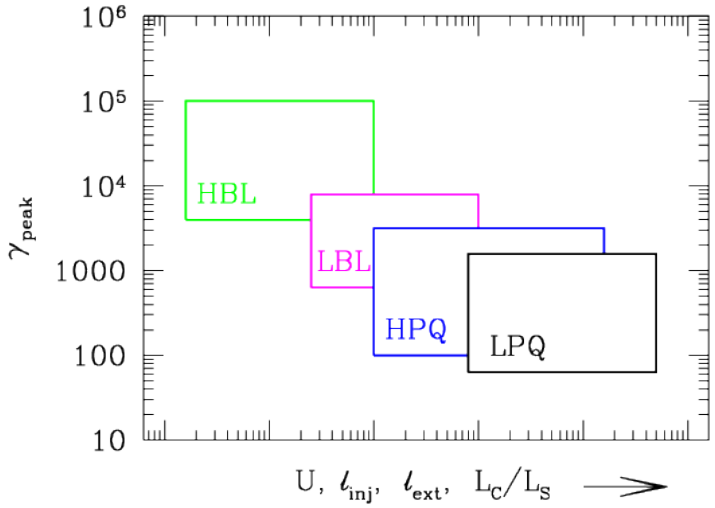

Figure 1.4: Unification for Blazars (Ghisellini et al., 1998)

that their spectra are governed by a single parameter, related to luminosity, which impacts the physical properties and radiation mechanisms in the jets (Fossati et al., 1998). Consequently, objects along this sequence are sorted primarily by the observed power. The classes are, in order of descending peak frequencies, high frequency BL Lac objects (HBL), low frequency BL Lac objects (LBL), highly polarized quasars (HPQ), and lowly polarized quasars (LPQ). This can be seen in Fig. 1.4.
Ghisellini et al. (1998) therefore propose a model that describes the differences along this sequence as due to an increasing importance of an external radiation field, that is, an increasing role of broad emission line radiation. This in turn means an increase in the total energy density and the injected power, which result in a decrease of γ_{peak}, which corresponds to the energy of electrons emitting at the peak of the observed spectra. However, the fundamental physical jet processes are believed to be the same for all blazar flavors.

1.3 The TANAMI project

The source sample analyzed in this thesis consists of sources monitored by the TANAMI project (short for Tracking Active Galactic Nuclei with Austral Milliarcsecond Interferometry). Under the leadership of R. Ojha and M. Kadler, this project has been studying parsec-scale structures and dynamics of AGN jets since November 2007. As it monitors sources south of -30 degrees declination, it can be seen as a complement to similar programs in the Northern Hemisphere such as MOJAVE (see, e.g., Lister et al., 2009). TANAMI observations are operated using the Australian/South-African Long Baseline Array (LBA+), which includes antennas at Parkes (64 m), ATCA (5×22 m), Mopra (22 m), Hobart (26 m), Ceduna (30 m) as well as the associated antennas Tidbinbilla (DSN 70 m or 34 m), the IVS antennas TIGO (6 m) and O'Higgins (9 m) and Hartebeesthoek (26 m). Monitoring frequencies are 8.4 GHz and 22 GHz (see Ojha et al., 2010a,b and the TANAMI homepage[1]).
The lower part of Fig. 1.5 gives an overview over the antennae used by TANAMI. The upper part of the figure shows an austral view of the gamma-ray sky in celestial coordinates as seen by *Fermi* as well as TANAMI VLBI jet images for selected sources. Figures 1.6 and 1.7 show examples for TANAMI observations of two sources analyzed in chapter 3. The images were derived from the 8.4 GHz data from the first TANAMI run in November 2007 by Ojha et al. (2010a).

[1] http://pulsar.sternwarte.uni-erlangen.de/tanami/

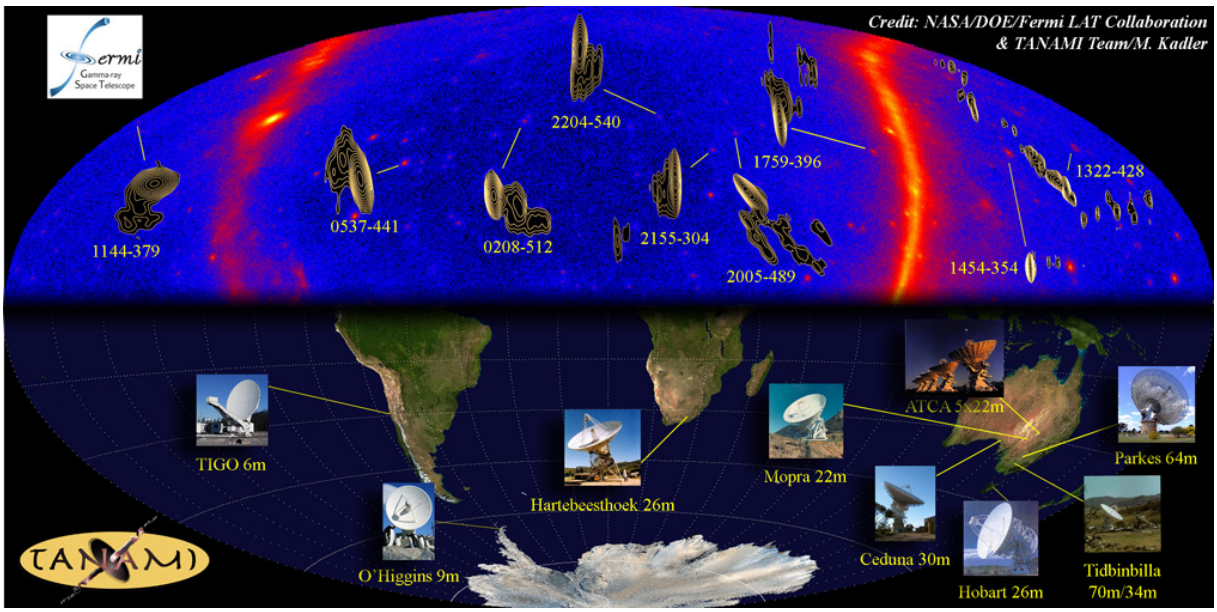

Figure 1.5: TANAMI (http://pulsar.sternwarte.uni-erlangen.de/tanami/)

Figure 1.6: 8.4 GHz image of PKS 1322−428
Credit: TANAMI (Ojha et al., 2010a)

Figure 1.7: 8.4 GHz image of PKS 2005−489
Credit: TANAMI (Ojha et al., 2010a)

One of the key goals of TANAMI is to discover the origin of gamma-rays in AGN jet spectra. An important question is, if gamma-ray flares are accompanied by jet-component ejections. For this reason, blazars flaring at gamma-rays, in particular those detected with *Fermi's* Large Area Telescope (LAT), are sources of special interest (e.g, Ojha et al., 2010a,b). For these sources, multiwavelength observations are aspired in order to obtain broadband SEDs. This shows the interest in collaboration with *Swift*, as the UVOT and XRT detectors offer broadband observations (see chapter 2) which supplement the available radio data from TANAMI and gamma-ray data from *Fermi* well.

Chapter 2

Data

2.1 *Swift*

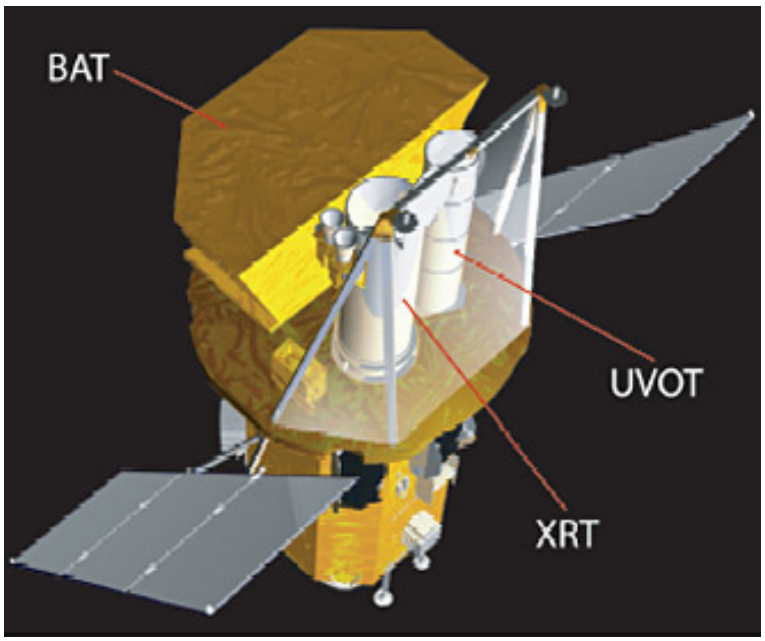

Figure 2.1: *Swift*, Credit: NASA/GSFC

All data were taken from observations of the *Swift* satellite, which is operated by the NASA Goddard Space Flight Center. Main goal of this multi-wavelength observatory, which was launched on November 20, 2004, is the study of gamma-ray bursts (GRB) (e.g., Gehrels et al., 2004). On April 13, 2010, *Swift* observed its 500th burst (NASA, 2010).
The first of *Swift's* three coaligned instruments is the Burst-Alert Telescope (BAT), a large-field-of-view (FOV) coded mask hard X-ray detector designed to detect and locate GRBs within seconds after an outburst. The observing strategy is for the satellite to repoint itself swiftly and independently so as to bring the burst location within the field of view of the other two instruments, the UltraViolet/Optical Telescope (UVOT) and the X-Ray Telescope (XRT), which are designed as sensitive instruments to measure the fluxes, spectra, and light curves of GRBs and their afterglows (e.g., Holland, 2010).

2.2 XRT

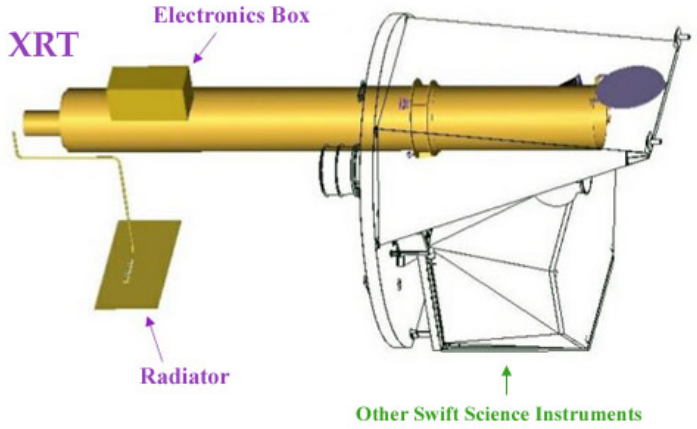

Figure 2.2: Scheme of *Swift's* XRT, Credit: NASA/GSFC

Table 2.1: XRT characteristics

Parameter	Value
Telescope	JET-X Wolter 1
Focal Length	3.5 m
Energy Range	$0.2 - 10$ keV
Effective Area	120 cm^2 at 1.5 keV
Detector	E2V CCD-22, 600×602 pixels
Readout Modes	Photon-counting, integrated imaging, and timing
Field of View	$23.6' \times 23.6'$
Telescope PSF	$18''$ HPD at 1.5 keV
	$22''$ HPD at 8.1 keV
Sensitivity	2×10^{-14} erg cm^{-2} s^{-1} in 10^4 s

All analyzed measurements were taken by the XRT, a 3.5 m Wolter type I telescope with a E2V CCD-22 detector. The energy range is specified as $0.2 - 10$ keV. Table 2.1 shows an overview of the most important instrument characteristics. The point spread function (PSF), which describes the telescope response to a point source, corresponding to angular resolution, is given in values of half power diameter (HPD). All specifications are taken from the *Swift* Technical Handbook (Holland, 2010).
Three major components contribute to the XRT effective area: the mirror effective area, the filter transmission and the CCD quantum efficiency (QE). The sensitive area or Ancillary Response File (ARF), contains the first two elements, as well as further correction terms depending on source location and the size of the extraction region. The QE is included in the spectral response or Redistribution Matrix File (RMF) (Campana et al., 2009). Both files are generated by NASA via Monte-Carlo simulation and distributed along with the *Swift* calibration database.
Figures 2.3 and 2.4 show the ARF and RMF files, respectively, for observation 00035242001 of PKS 2149−306. Several detector features are visible in the ARF: Major absorption features can be seen at approximately 0.5 keV (due to an oxygen transition in the detector surface), 1.5 keV (aluminum feature originating from the filter) and 1.8 keV (caused by a silicon K-shell

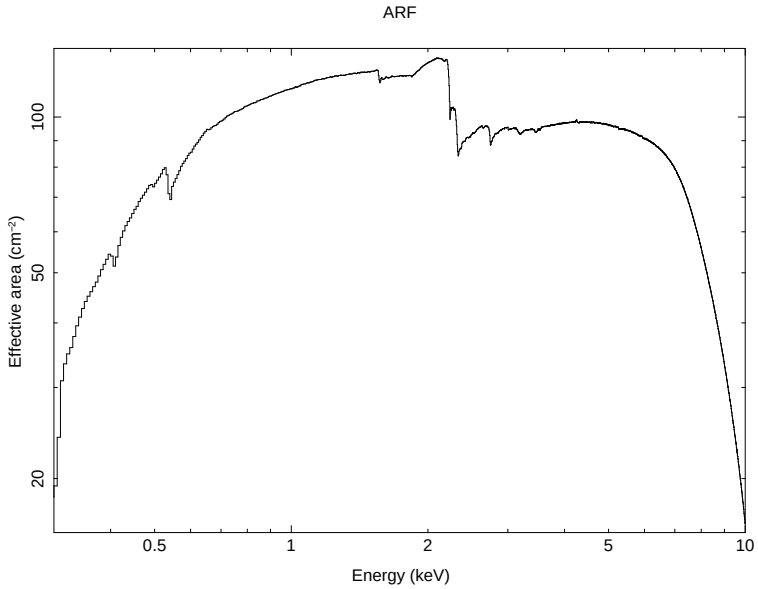

Figure 2.3: Ancillary Response

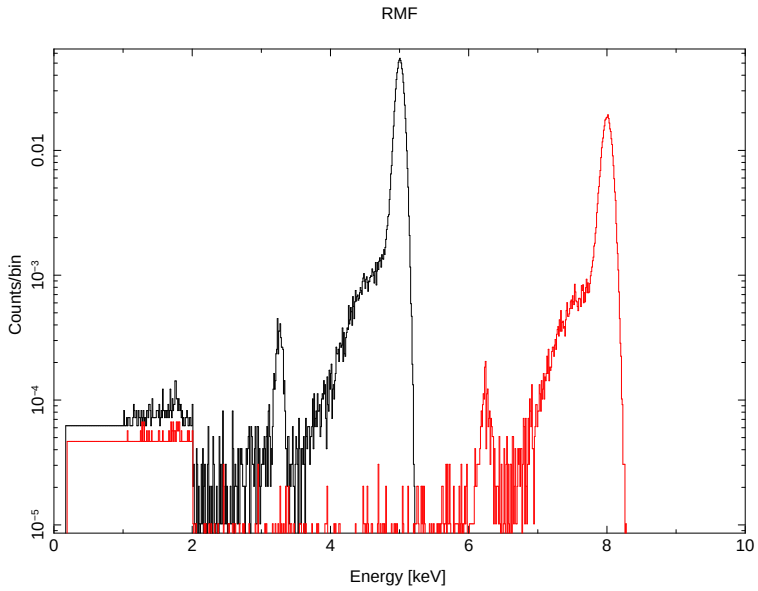

Figure 2.4: Redistribution matrix for initial energies of 5 (black) and 8 keV (red)

transition in the detector material, see Campana et al., 2009). The edge at 2.2 keV is caused by a change in the reflectivity of the telescope mirrors and can be attributed to the M-shell transition in the gold mirror material.
The RMF is plotted for initial photon energies of 5 (black) and 8 keV (red) respectively. The redward slopes of the main response peaks show a Compton shoulder, which originates from the Compton backscattering of photons. In addition, an escape peak with an energy of 2 keV less than the initial photon energy can be seen. This peak is caused by fluorescence photons of the K transition. Every time a fluorescence photon leaves the camera undetected, the measured photon energy is reduced by the resonance energy of the transition, which is characterized by said 2 keV (see also Krauß, 2010).

The available observations were all in the photon-counting mode, which retains full imaging and spectroscopic resolution. The readout time of 2.5 s is however a problem for medium to strong fluxes, as pileup can occur. This is the case, when more than one photon arrive at the same pixel between two read-outs. As the CCD only measures the total deposited charge,

it cannot differentiate between one high-energetic photon and two less energetic photons. Therefore, this effect has to be taken into account and corrected for very strong sources.
A better mode for obtaining spectra of bright sources is the windowed timing mode, which sacrifices position information to achieve a high time resolution by means of rapid CCD readouts (readout time 2.2 ms). However, no observations in this mode were available for analysis.

2.3 Sample selection

The initial TANAMI sample includes 44 sources. It is a combination of mainly two subsamples: a radio selected and flux-density limited ($S_{5\,\mathrm{GHz}} > 2\,\mathrm{Jy}$) subsample with flat radio spectra between 2.7 GHz and 5 GHz on one hand, and a gamma-ray selected subsample including all known gamma-ray blazars detected by EGRET south of $\delta = -30^\circ$ on the other hand. In November 2008, 19 additional sources of interest that had been observed by the *Fermi* satellite were added to the sample. As of June 2010, the current TANAMI sample includes 75 sources, 55 of which have been detected by *Fermi*.
For analyzing the *Swift* data, the TANAMI source sample was divided into two subsamples according to the sources' right ascension α. The targets analyzed in this thesis lie in the range of $07^\mathrm{h} < \alpha < 24^\mathrm{h}$. Within these coordinates, *Swift* observations for 26 TANAMI sources were available. The second subsample, including sources with $00^\mathrm{h} < \alpha < 07^\mathrm{h}$, was analyzed by Krauß (2010). The results of the two samples are compared in section 4.3.

2.4 Data reduction

Before analyzing, the raw data had to be reduced to obtain spectra. For this, scripts written by L. Barragán (ECAP) were available. In a first step, the raw data had to be prepared, that is, bad pixels were eliminated and other corrections applied. In a second step, a first image of the full FOV was extracted, which could be viewed by means of the program ds9. Via a script written by J. Wilms, source information could be imported from SIMBAD, which made the identification of the requested source and other sources visible on the image possible.
The crucial factor was the determination of source and background regions. The source region was determined as a circular area including all discernible counts. For very strong sources, pile-up was corrected for by excluding the central pixels. As background, a region of the same size, in which no apparent point sources were present, was chosen. In a last step, all photon information was subsequently extracted from the specified regions to gain the desired background subtracted spectra.
Examples of source and background regions are shown in Fig. 2.5 for a strong and Fig. 2.6 for a weak source.

2.5 Data analysis

The background subtracted spectra were then processed and plotted with ISIS (see Houck & Denicola, 2000). As can be seen in Fig. 2.7, some sources yielded only very weak spectra, which could not be further analysed (see section 3.2 for details). For strong sources, the raw spectra were rebinned to diminish the noise by setting the minimum signal-to-noise ratio to a value of 5. This step is depicted in Fig. 2.8 and Fig. 2.9, showing the spectrum of PKS 2005−489 before and after the rebinning, respectively.
For some sources, several observations from the same epoch were available. These were

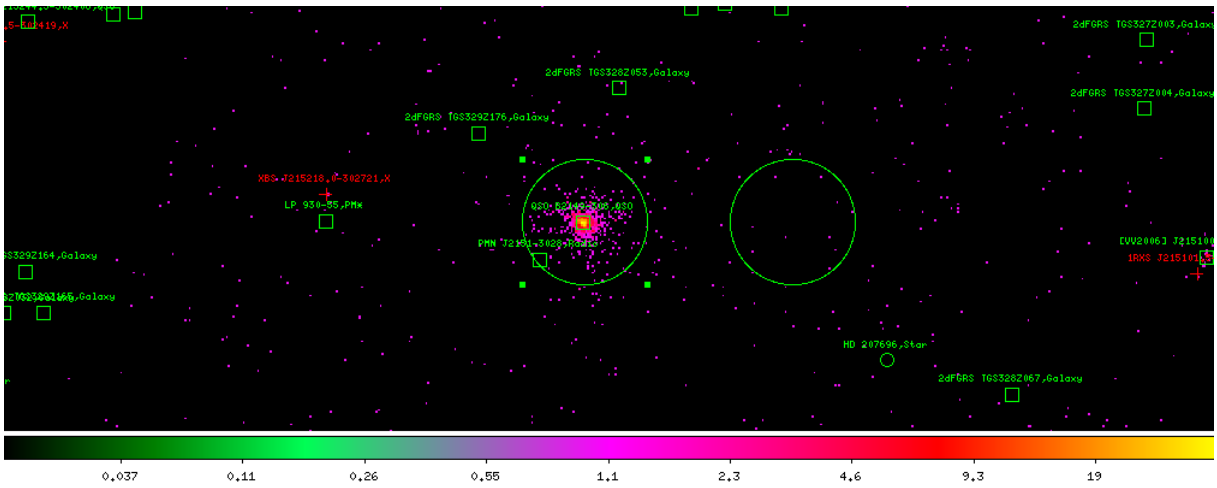

Figure 2.5: Source and background regions for PKS 2149−306

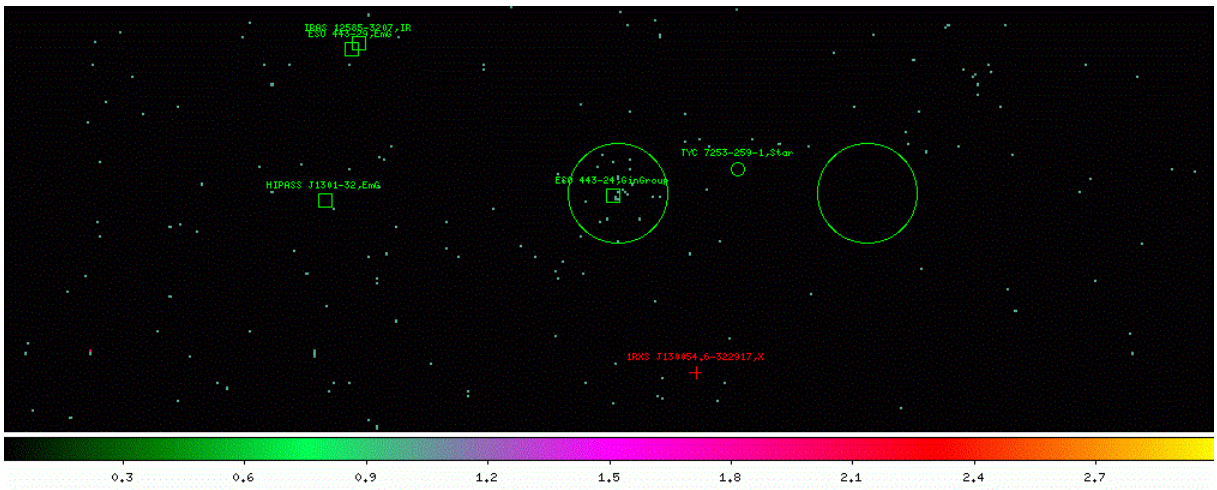

Figure 2.6: Source and background regions for PKS 1257−326

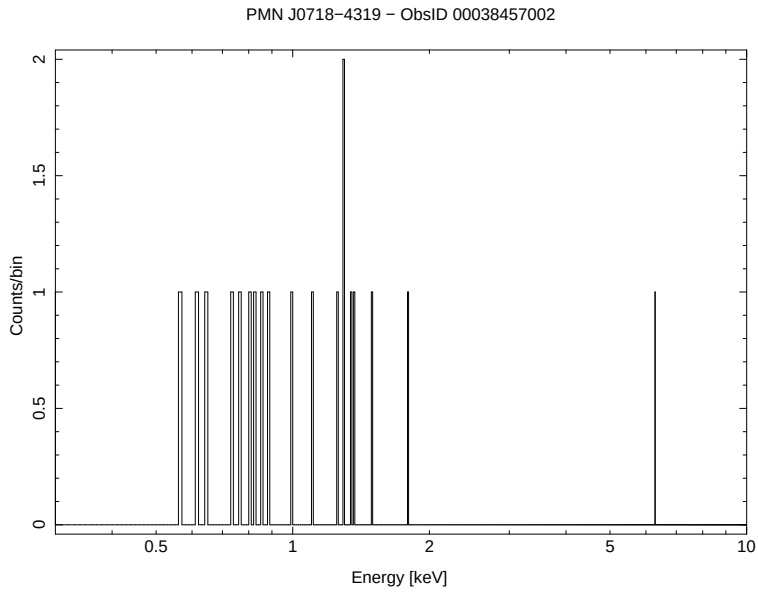

Figure 2.7: Spectrum of PMN J0718−4319

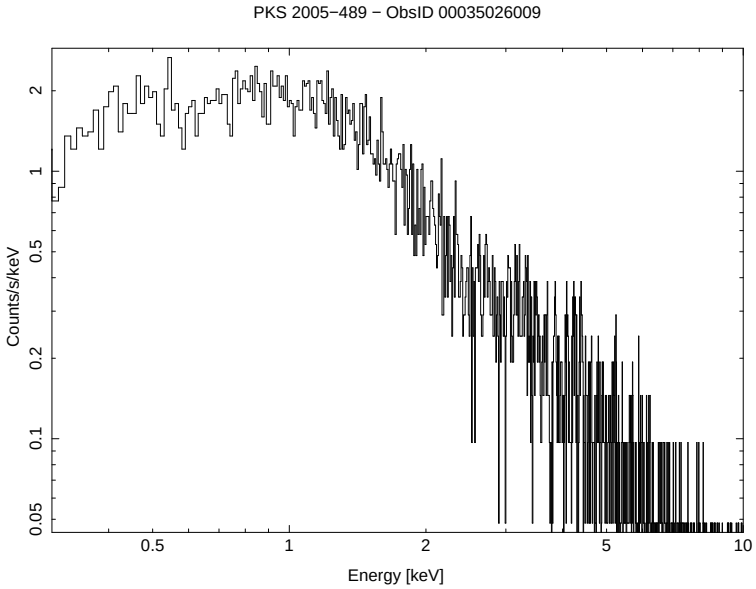

Figure 2.8: Spectrum of PKS 2005−489 before rebinning

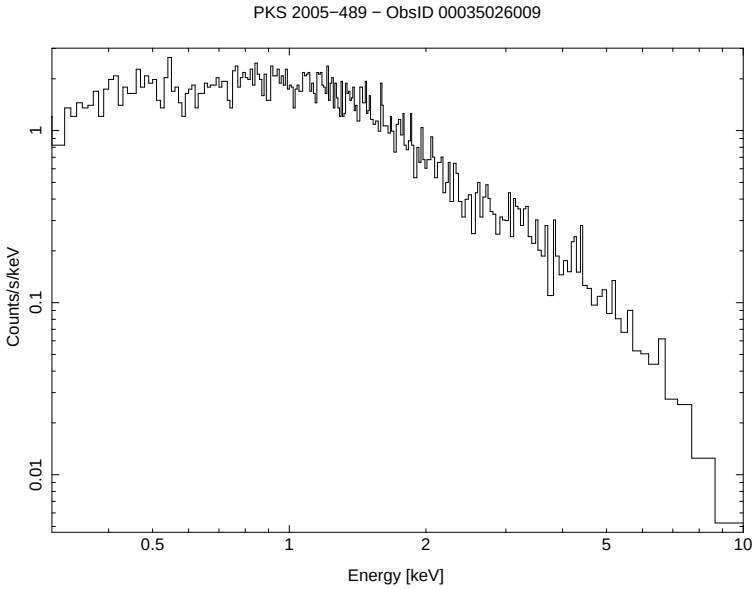

Figure 2.9: Spectrum of PKS 2005−489 after rebinning

grouped into added spectra with the phaadd command to obtain stronger spectra and, in consequence, a higher spectral resolution after rebinning. All observations IDs are listed in the appendix (Tables I, II, and III). For each source, a total added spectrum was compiled. If further spectra including only some of the observations of one source were added, the spectrum number is listed.
The energy range was limited to a rather large interval of $(0.3-10)$ keV. This has to be kept in mind when looking at the modeled spectra. Slight deviations between the model and the observed spectra are likely to occur at very high or very low energies. These deviations can be attributed to larger uncertainties which arise mainly due to smaller effective areas in these energy ranges.
As a fit function for most sources, a power law model with a photoabsorption component was chosen as follows:

$$N_{ph}(E) = e^{-N_{\mathrm{H}} \cdot \sigma_{\mathrm{ism}}} \cdot C \cdot E^{-\Gamma} \tag{2.1}$$

Here, C is the norm of the power-law, and $\Gamma = 1 + \alpha$ describes the photon index. The exponential function describes the absorption in the interstellar medium (ISM), which is characterized by the cross-section σ_{ism} per Hydrogen atom for matter of solar composition as well as by the hydrogen column density N_{H}.
For each spectrum, two fits were performed. For the first one, the three model parameters Γ, C and N_{H} were variable. For the second fit, the N_{H} parameter was fixed to the Galactic absorption values, which were taken from the Leiden/Argentine/Bonn Galactic HI Survey (Kalberla et al., 2005). The results of the two models (fixed vs. free N_{H}) are compared in section 4.2.
For two sources, more specifically PKS 1322-428 (which is Centaurus A) and PKS 1333-336, an expanded model had to be applied as they exhibit so-called partial coverers. This means that the spectrum is partially absorbed by obscuring material, mostly dust bands, in the underlying host galaxy. This was accounted for by adding an additional absorption component to the fit function as follows:

$$N_{ph}(E) = e^{-N_{\mathrm{H},1}\cdot\sigma_{\mathrm{ism}}} \cdot C \cdot E^{-\Gamma} \cdot \left[1 + f \cdot e^{-N_{\mathrm{H},2}\cdot\sigma_{\mathrm{ism}}}\right] \tag{2.2}$$

The fit function can be interpreted as two components of the same power-law spectrum, one absorbed internally and one not absorbed, passing through the interstellar medium and therefore both being absorbed externally. The inner absorption component is characterized by the coefficient $N_{\mathrm{H},2}$ as well as a constant f. For both sources, the external absorption coefficient $N_{\mathrm{H},1}$ was fixed to the Galactic value, respectively. This is helpful, as it compensates fairly well for the uncertainties that arise because the inner absorption process cannot be assumed to be due to a cold absorber alone. For better modeling, warm absorber components, that by consequence will become transparent below a threshold energy, have to be included.
For all strong sources, tables with the obtained fit-parameters are given in chapter 3. All error bars in the plots describe 90% confidence levels, as do the given parameter errors. For some sources, several spectra could be modeled. Independent parameter values were derived for each fitted spectrum. Overall parameters for each source were determined as average of the obtained values. For this purpose, Gaussian error propagation was applied.

The measured spectra give the number of counts per channel as $\mathrm{Counts\,s^{-1}\,keV^{-1}}$. These measured spectra can differ strongly from the spectra arriving at the detector from the radiation source, as the measured spectra are a convolution of the source flux with the detector response and effective area combined with a background signal. This relation cannot be inverted to extract the initial source flux. So-called “unfolded” spectra can be acquired numerically, e.g., with ISIS, to get an impression of the real source spectrum. However, they have to be handled with caution, as detector features can easily be wrongly interpreted as spectral features (Nowak, 2009). Unfolded spectra are shown in section 3.1 for PKS 1322−428 and PKS 2155−304.

Chapter 3

Observations

3.1 Strong sources

In this chapter, all deduced information on each source is given, which includes spectra as well as fit parameters. Numbers in parentheses give the IAU 1950 name for sources not found in the PKS catalogue. In addition, an overview of the general source properties – as far as available – is given. These include the Galactic N_{H} values from the Leiden/Argentine/Bonn Galactic HI Survey (Kalberla et al., 2005) as well as source type, coordinates, and redshift values from the NASA/IPAC Extragalactic Database (NED). Coordinates are given in the format right ascension, declination (J2000). Distances, also from NED, are only given if redshift independent measurements have been performed.
Fit parameter tables are given for all sources. The stated values are the free fit parameters C, Γ in units of 1, and N_{H} in units of $10^{22}\,\mathrm{cm}^{-2}$, as well as the reduced χ^2-parameters for fits with free and fixed ("red. χ^2 (N_{H})") photoabsorption. In addition, the exposure time t and the degrees of freedom (DOF), that is the number of bins after the rebinning process minus the number of variable fit parameters, are given for each spectrum.

PMN J0810−7530 (0812-736)

PMN J0810−7530 is a radio source that was detected with the Parkes-MIT-NRAO (PMN) radio continuum survey. Not much has been published about it.

Table 3.1: Overview

Source name	PMN J0810−7530
Coordinates	122.75917, −75.51097
Galactic N_{H}	$0.0194 \cdot 10^{22}\,\mathrm{cm}^{-2}$
z	?
d	?
Type	?

Six observations made over a timespan of two weeks were available. Out of these, 00038459001 could be modeled individually, while the other observation IDs yielded only very bad fits. For this reason, all observations were added to obtain the total added spectrum as seen in the figure.

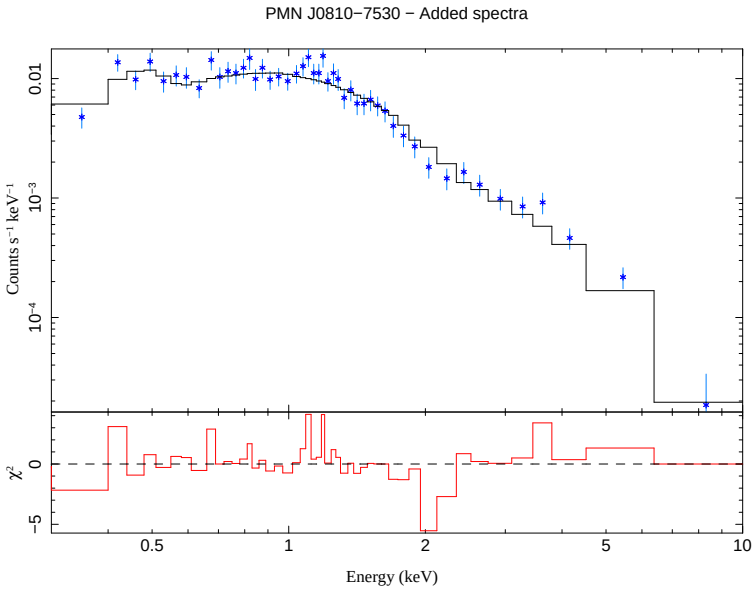

In addition, the spectra of the first and second weeks of observation respectively were added separately to obtain added spectra #1 and #2, which were used to calculate the average values.

Table 3.2: Fit parameters

Observation	t [ks]	DOF	N_{H}	C [10^{-4}]	Γ	red. χ^2	red. χ^2 (N_{H})
00038459001	26.65	16	$0.19^{+0.09}_{-0.07}$	$2.2^{+0.8}_{-0.6}$	$2.7^{+0.4}_{-0.3}$	0.8419	2.2073
Added #1	52.31	32	$0.14^{+0.05}_{-0.04}$	$2.0^{+0.4}_{-0.3}$	2.6 ± 0.2	0.8776	1.9909
Added #2	31.71	21	$0.15^{+0.07}_{-0.05}$	$2.1^{+0.6}_{-0.4}$	$2.7^{+0.4}_{-0.3}$	1.5767	2.5465
Added	84.02	49	$0.15^{+0.04}_{-0.03}$	2.2 ± 0.3	2.7 ± 0.2	1.0424	2.4805
Average			0.15 ± 0.04	2.1 ± 0.3	2.7 ± 0.2		

PKS 1057−797

This source has been classified as a BL Lac with weak emission lines, from which a redshift was determined by Sbarufatti et al. (2009).

Table 3.3: Overview

Source name	PKS 1057−797
Coordinates	164.6804571, −80.0650442
Galactic N_{H}	$0.0147 \cdot 10^{22}\,\mathrm{cm}^{-2}$
z	0.569
d	?
Type	BL Lac

For PKS 1057−797, three observations were available, all of which were rather weak. However, the total added spectrum yielded fairly good fit results. The data was taken over a timespan of roughly a month.

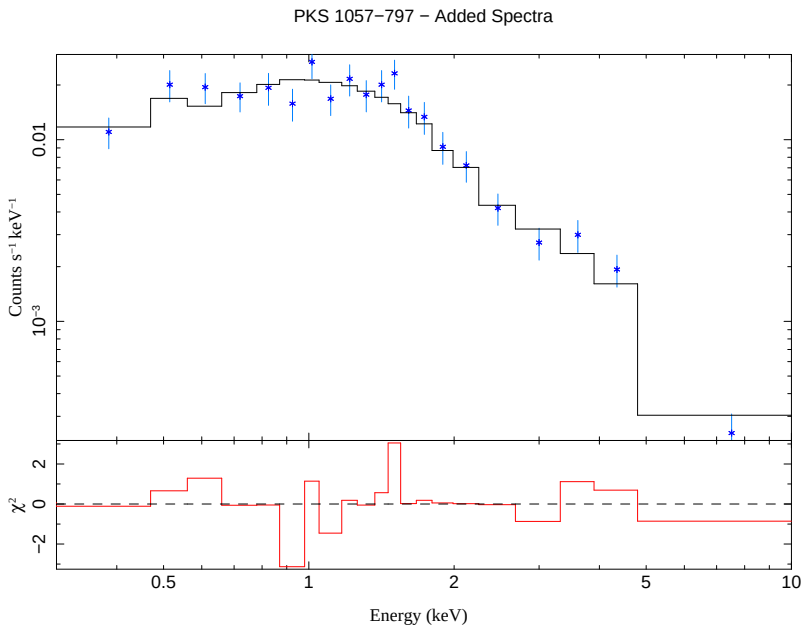

Table 3.4: Fit parameters

Observation	t [ks]	DOF	N_{H}	C [10^{-4}]	Γ	red. χ^2	red. χ^2 (N_{H})
Added	14.39	22	$0.13^{+0.06}_{-0.05}$	$4.0^{+0.9}_{-0.7}$	2.1 ± 0.2	0.7976	1.7324

PKS 1313−333

This flat-spectrum QSO has been studied in the radio and Gamma-rays bands (e.g., Nolan et al., 1996). From observation in the *ROSAT* All-Sky Survey, an upper limit for its flux in the $0.1-2.4$ keV X-ray band was derived as $F_x < 0.453 \cdot 10^{-12}$ erg cm^{-2} s^{-1} by Siebert et al. (1998).

Table 3.5: Overview

Source name	PKS 1313−333
Coordinates	199.0332746, −33.6497697
Galactic N_{H}	$0.0331 \cdot 10^{22}$ cm^{-2}
z	1.21
d	?
Type	QSO

For PKS 1313−333, only one observation was available.

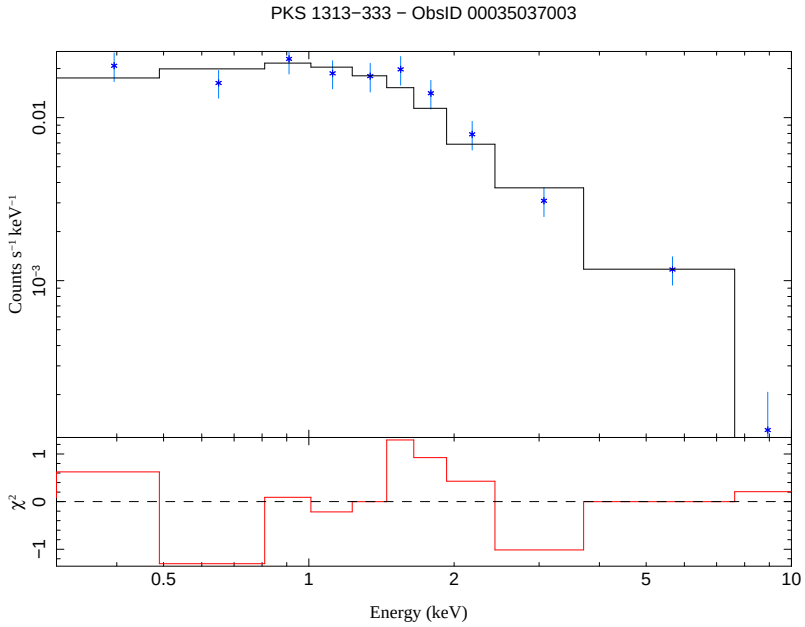

Table 3.6: Fit parameters

Observation	t [ks]	DOF	N_{H}	C [10^{-4}]	Γ	red. χ^2	red. χ^2 (N_{H})
00035037003	6.32	12	$0.04^{+0.08}_{-0.04}$	$3.3^{+1.2}_{-0.8}$	1.8 ± 0.3	0.6571	0.5977

PKS 1322−428

This very bright source is better known as Centaurus A. As the nearest AGN, it has been well studied throughout the wavebands. It can be classified as a FR Type I source in the radio and as a Seyfert 2 in the optical range. There have been observations of an X-ray-jet (Hardcastle et al., 2003). However, no jet could not be resolved in our observations. In the year of 2009, PKS 1322−428 was detected in the VHE regime ($E > 100\,\mathrm{GeV}$) with H.E.S.S. (Aharonian et al., 2009).

Table 3.7: Overview

Source name	PKS 1322−428
Coordinates	201.3650633, −43.0191125
Galactic N_{H}	$0.0477 \cdot 10^{22}\,\mathrm{cm}^{-2}$
z	0.001825
d	3.6 Mpc
Type	Seyfert 2

As the source is known to have strong central absorption due to a dust band in the underlying galaxy, an extended model was applied. The absorption coefficient for external absorption was held constant at the Galactic value. The intrinsic absorption coefficient $N_{\mathrm{H,int}}$ is given in units of [$10^{22}\,\mathrm{cm}^{-2}$]. For PKS 1322−428, an unfolded spectrum was plotted in addition to the measured spectrum. One can clearly see a rising spectra, which is in agreement with the fitted photon index of $\Gamma = 1.30 \pm 0.13$.

The rst added spectrum consists of two observations taken in August 2005. The second added spectrum is composed of four observations from May 2007.

Table 3.8: Fit parameters

Observation	t [ks]	DOF	$N_{H;int}$	C [10 ^{2}]	G	red. c^2	red. c^2 (N_H)
Added #1	10.05	321	11:1 0:5	$4:3^{+0:8}_{0:7}$	1:39 0:09	1.3069	1.3059
Added #2	1.66	75	$11:4^{+1:5}_{1:4}$	$3:0^{+2:0}_{1:0}$	$1:2^{+0:2}_{0:3}$	1.2395	1.2329
Average			11:3 0:8	3:6 0:9	1:30 0:13		

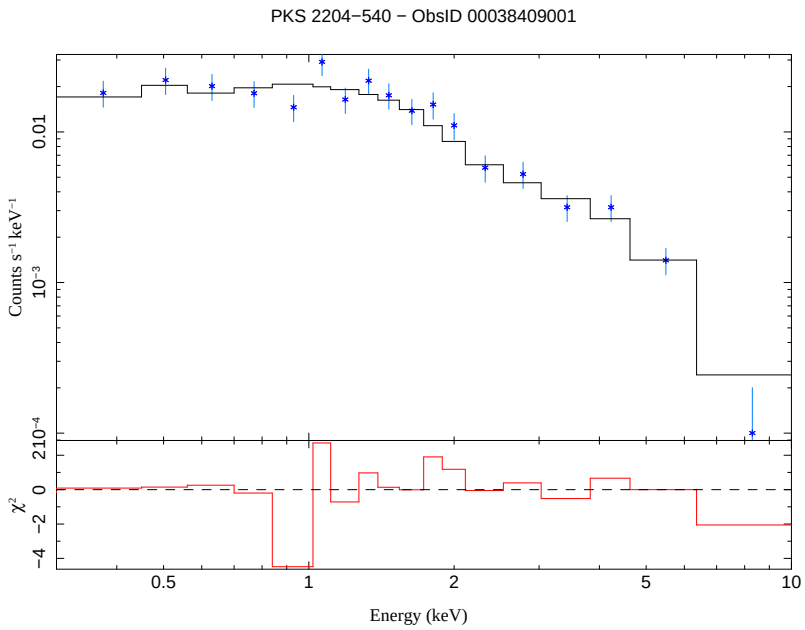

Table 3.26: Fit parameters

Observation	t [ks]	DOF	N_H	C [10^{-4}]	Γ	red. χ^2	red. χ^2 (N_H)
00038409001	10.29	19	$0.02^{+0.05}_{-0.02}$	$2.8^{+0.6}_{-0.4}$	1.6 ± 0.2	1.0142	0.9599

3.2 Weak sources

Table 3.27: Weak sources (n.d. = not determinable)

Source	Type	t [ks]	stn-ratio	Obs. period [d]	Γ	red. χ^2
PMN J0718−4319	?	21.11	10.38		n.d.	
PKS 1144−379	HP QSO	5.18	9.71		n.d.	
PKS 1424−418	HP QSO	7.58	19.79	425	1.4 ± 0.2	1.02
PKS 1454−354	QSO	10.61	15.81	249	$1.8^{+0.4}_{-0.3}$	0.80
PMN J1802−3940	?	11.90	15.29	346	1.8 ± 0.3	1.35
PKS 1954−388	HP QSO	6.34	17.54	371	1.8 ± 0.3	1.45
PMN J2139−4235	BL Lac	6.41	8.20		n.d.	
PKS 2355−534	QSO	42.64	19.24	1191	$1.7^{+0.3}_{-0.2}$	0.74

Apart from the before mentioned strong sources, eight further objects could be significantly detected. These weak sources had low countrates, which in the attempt of spectral fitting yielded rather bad fits. For PKS 1424−418, PKS 1454−354, PMNJ 1802−3940, PKS 1954−388, and PKS 2355−534 models were fitted to the total added spectra, which yielded fairly good results. One should, however, keep in mind that the added spectra consist of observations separated by long periods of time and that these sources are variable. As can be seen in Table 3.27, four of the photon indices are in the range of $\Gamma \approx 1.8$, which could indicate similar source types. We indeed find that three of the weak sources have been identified as high-peaked QSOs. This seems reasonable, as these sources are expected to have a low flux in the X-ray band.
For the sources PMN J0718−4319, PKS 1144−379 and PMN J2139−4235, individual modeling was not possible. To get a rough impression of the range their spectral parameters lie

in, the three sources were combined into one added spectrum. With the data being grouped to a minimum stn-ratio of $stn \geq 2$, this allowed for spectral fitting. The fit yielded a photon index of $2.3^{+0.5}_{-0.3}$, a power-law norm of $(0.7^{+0.2}_{-0.1}) \times 10^{-4}$, and an absorption coefficient of $0.03^{+0.07}_{-0.03} \cdot 10^{-22}\,\mathrm{cm}^{-2}$ at a χ^2 value of 0.60.

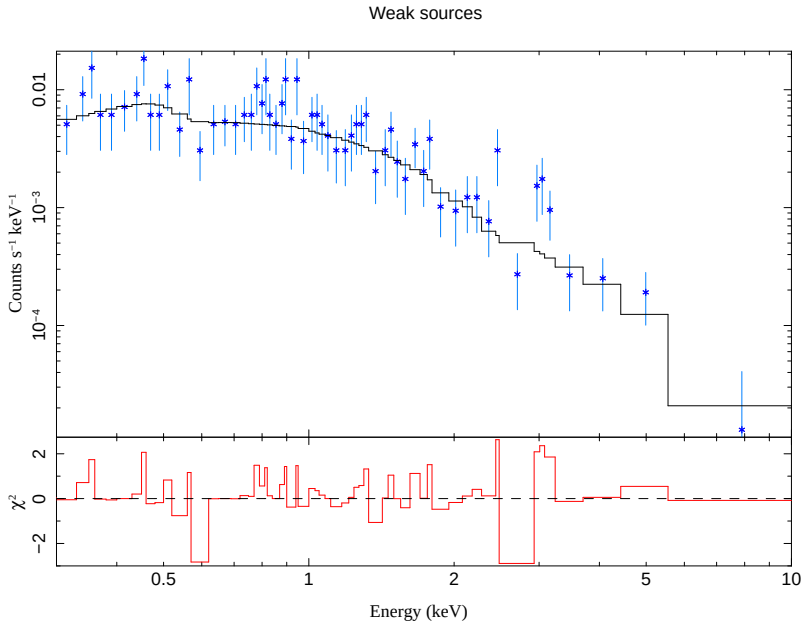

3.3 Not detected sources

Among the monitored sources, PKS 0736−770, PKS 1257−326, PMN J1347−3750, PMN J1603−4904, and PKS 2027−308 couldn't be significantly detected. The underlying criteria is the achieved signal-to-noise ratio of the total added spectrum of each souce. If the total stn-ratio is smaller than 5, this means less than 5σ confidence level for the source detection. A look at the total exposure times (the sum of all observations) and the achieved stn-ratios suggests that further observation could probably yield significant detections.

Table 3.28: Not detected sources

Source	Type	t [ks]	stn-ratio
PKS 0736−770	QSO	6.92	4.20
PKS 1257−326	QSO	2.10	4.69
PMN J1347−3750	?	0.63	2.45
PMN J1603−4904	?	0.75	3.00
PKS 2027−308	Galaxy	5.01	1.39

Like for the weak sources (see sec. 3.2), the spectra of all not detected sources were added to get a rough impression of the range their spectral parameters lie in. Again the data were grouped to a minimum stn-ratio of $stn \geq 2$. The fit yielded a photon index of $2.1^{+1.1}_{-0.7}$ and an absorption coefficient of $0.2^{+0.3}_{-0.2} \cdot 10^{-22}\,\mathrm{cm}^{-2}$ at a χ^2 value of 0.16. The power-law norm could not be determined as the errors were too large.

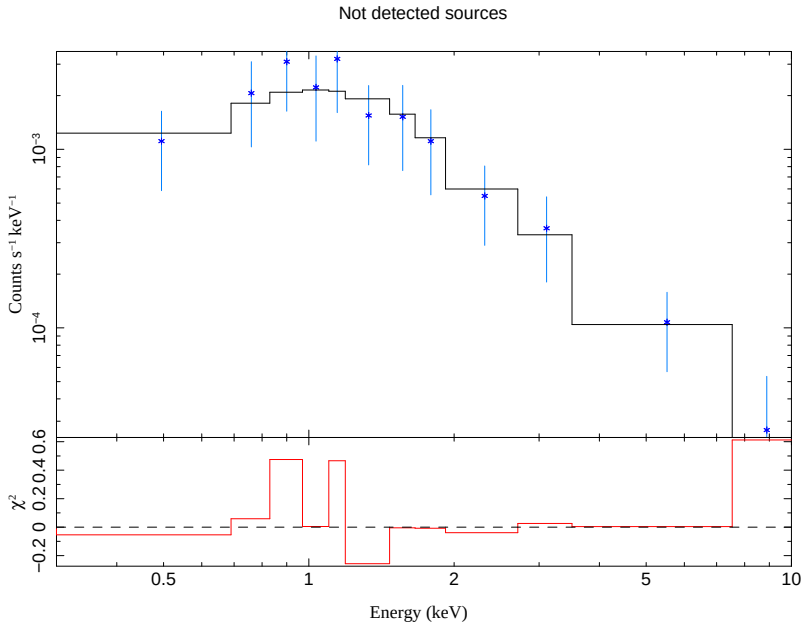

3.4 USNOA2 0525−42507178

While monitoring PKS 2027−308, another interesting object was detected inside the FOV. This source was significantly detected (signal-to-noise ratio 6.25). The coordinates were determined as approximately (307.60833, −30.63600). By comparing these to a map of the DSS (Digital Sky Survey), it was possible to identify the object with the optical counterpart USNOA2 0525−42507178. Nothing else is known about this source. As there were very few measured counts, the attempt to fit a spectrum was not successful.

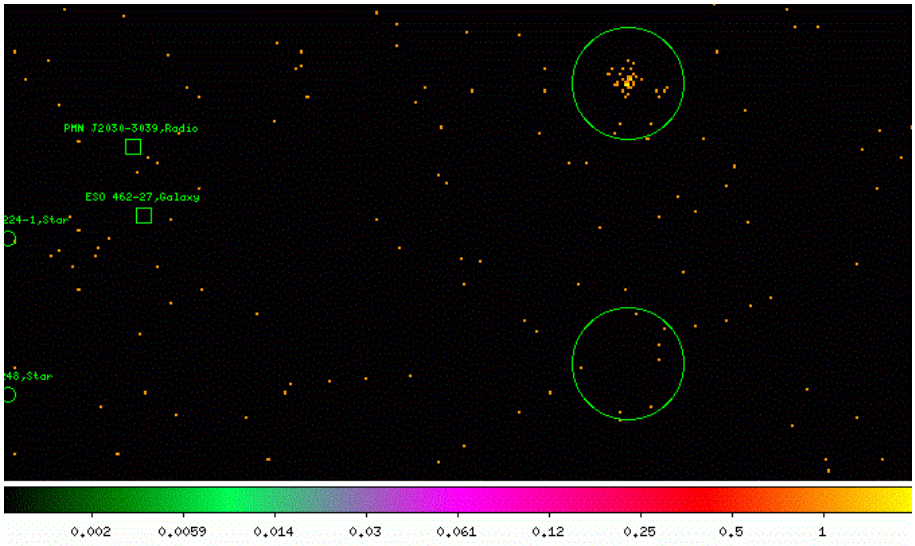

Figure 3.1: Source and background regions for USNOA2 0525−42507178

Chapter 4

Results

4.1 Photon indices

Table 4.1: Photon indices

Source	Source type	Γ
PMN J0810−7530	?	2.7 ± 0.2
PKS 1057−797	BL Lac	2.1 ± 0.2
PKS 1313−333	QSO	1.8 ± 0.3
PKS 1322−428	Seyfert 2	1.30 ± 0.13
PMNJ 1326−5256	?	1.6 ± 0.3
PKS 1333−336	LINER	2.52 ± 0.05
PKS 1440−389	?	2.81 ± 0.14
PKS 1549−790	Seyfert 1	1.8 ± 0.3
PKS 2005−489	BL Lac	2.55 ± 0.05
PKS 2052−474	QSO	1.61 ± 0.15
PKS 2149−306	QSO	1.40 ± 0.05
PKS 2155−304	HP BL Lac	2.50 ± 0.03
PKS 2204−540	QSO	1.6 ± 0.2
PKS 1424−418	HP QSO	1.4 ± 0.2
PKS 1454−354	QSO	$1.8^{+0.4}_{-0.3}$
PMN J1802−3940	?	1.8 ± 0.3
PKS 1954−388	HP QSO	1.8 ± 0.3
PKS 2355−534	QSO	$1.7^{+0.3}_{-0.2}$

Table 4.1 shows an overview of all measured photon indices, both of strong and weak sources. A histogram is shown in Fig. 4.1. Clearly visible are the two accumulations around photon indices of approximately 1.7 and 2.7, respectively, as well as a deficiency of sources between these two peaks. This is in good agreement to our expectations, which state that sources with intermediate photon indices, corresponding to flat or slightly rising spectra, will exhibit a flux minimum in the monitored frequency range (see section 1.2). We also find that more low-frequency peaked sources ($\Gamma \approx 1.7$) than high-frequency peaked sources ($\Gamma \approx 2.7$) are observed. This effect is a logical consequence of low-frequency peaked sources being more luminous than high-frequency peaked sources. An additional bias is introduced by the TANAMI sample selection, as this sample is dominated by radio-selected sources. This means more FSRQs and low-frequency peaked BL Lacs are being observed than high-frequency peaked BL Lacs.

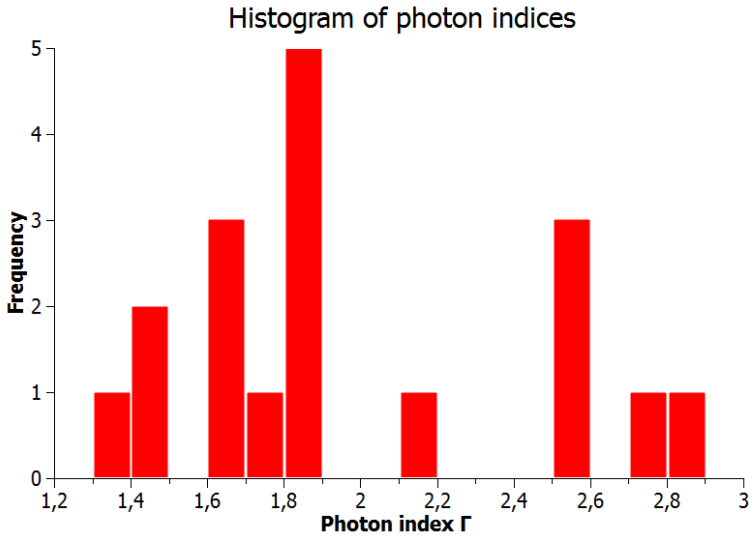

Figure 4.1: Distribution of photon indices

4.2 Absorption coefficients

Table 4.2: Absorption coefficients

Source	N_{H} $[10^{22}\,\mathrm{cm}^{-2}]$	$N_{\mathrm{H},gal}$ $[10^{22}\,\mathrm{cm}^{-2}]$
PMN J0810−7530	0.15 ± 0.04	0.0194
PKS 1057−797	$0.13^{+0.06}_{-0.05}$	0.0147
PKS 1313−333	$0.04^{+0.08}_{-0.04}$	0.0331
PKS 1322−428	$N_{\mathrm{H,int}} = 11.3 \pm 0.8$	0.0477
PMNJ 1326−5256	$0.25^{+0.11}_{-0.09}$	0.0345
PKS 1333−336	$N_{\mathrm{H,int}} = 2.0 \pm 0.1$	0.0569
PKS 1440−389	0.17 ± 0.03	0.033
PKS 1549−790	$3.8^{+0.8}_{-0.7}$	0.0196
PKS 2005−489	0.062 ± 0.007	0.0258
PKS 2052−474	0.06 ± 0.04	0.0295
PKS 2149−306	0.03 ± 0.01	0.0593
PKS 2155−304	0.022 ± 0.004	0.0605
PKS 2204−540	$0.02^{+0.05}_{-0.02}$	0.0137

Table 4.2 shows an overview over the measured absorption coefficients as well as the Galactic values of the hydrogen column density taken from the Leiden/Argentine/Bonn Galactic HI Survey. Three sources were modeled with a fixed Galactic absorption.
The Galactic values are in the range of a few $10^{20}\,\mathrm{cm}^{-2}$. The measured values tend to be slightly higher, ranging from several $10^{20}\,\mathrm{cm}^{-2}$ to several $10^{21}\,\mathrm{cm}^{-2}$. Intrinsically absorbed sources show higher values. The most interesting effect is seen for PKS 1549−790, which features an absorption coefficient of $3.8^{+0.8}_{-0.7}$. As discussed in section 3.1, this can be attributed to additional absorption effects linked to the optical extinction of this source.

4.3 AGN statistics

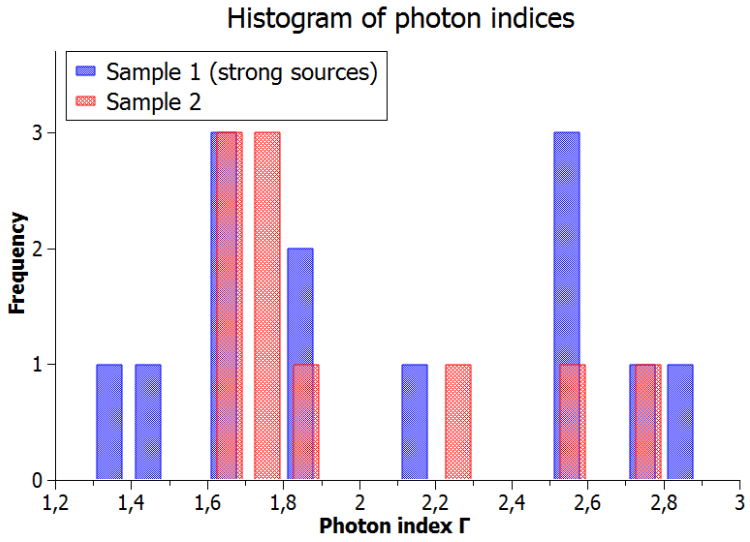

Figure 4.2: Distribution of photon indices

As a last step, the source sample discussed in this thesis (from now on referred to as sample 1) was compared to a source sample analyzed by F. Krauß (from now on referred to as sample 2) (see Krauß, 2010 for details). Both samples consist of TANAMI-observed sources, with the sample analysed by F. Krauß including sources between 0h and 7h right ascension and this sample including sources between 7h and 24h right ascension.
An interesting aspect is the number of detected sources relative to the number of observed sources. In sample 2, 10 out of 23 targets were observed as strong sources. No photon indices were derived for any of the sources classified as weak, which include sources equivalent to the "not detected" class in sample 1. For these reasons, only the strong sources of sample 1 were used for comparison. As there are 13 modeled source spectra out of 26, a value which is consistent with the fraction of analyzed sources in sample 2, we conclude that this selection is valid. Figure 4.2 shows the selected distribution of photon indices in both samples.
The two distributions were tested by method of a two-sample Kolmogorov-Smirnov test, which is used to test the null hypothesis, that both samples originate from the same probability distribution. This is done by comparing the maximum (absolute) difference of the two empirical distribution functions $D_{m,n} = \sup_x \left|F_{1,m}(x) - F_{2,n}(x)\right|$ to a critical value K_α, which describes the rejection level α (or acceptance level $1-\alpha$, respectively) of the null hypothesis. For our samples, we find a maximum difference of 0.284615 for samples sizes $m = 13$ and $n = 10$ respectively. The two samples can thus be assumed to be originating from the same probability distribution at $\approx 75\%$ confidence level.
For this reason, both samples were combined to obtain an overall distribution of photon indices. This is depicted in Fig. 4.3.

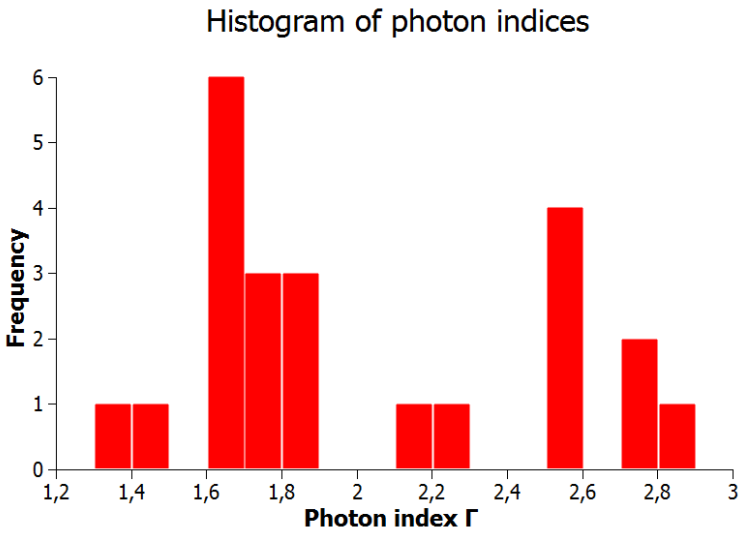

Figure 4.3: Histogram: complete sample

Chapter 5

Summary and outlook

The aim of this thesis was to study X-ray spectra of AGN from the TANAMI sample taken with the *Swift*/XRT. The performed spectral fits show that a simple photoabsorption $\times$ powerlaw model describes the observed spectra well. For some sources, an additional absorption component due to partial covering had to be applied. For PKS 2155−304, a broadband SED could be compiled. A simple fit of two parabolas yielded peak-frequencies that are in agreement to the derived X-ray photon index.
The comparison of this source sample to a supplementary sample analyzed by Krauß (2010) shows an overall agreement in the distribution of photon indices. The Kolmogorov-probability for both samples to arise from the same source distribution was calculated as $\approx 75\,\%$. This is a good sign, as no major differences between the two samples are to be expected.
Some sources could not be modeled as the measured spectra were too weak. In the future, more sensitive observations of blazars will be necessary to detect even the fainter objects in the X-ray band. On this subject, we look forward to the eROSITA project. These more sensitive observations will be needed to gain a better understanding of this subclass of AGN and to understand the physical processes causing these spectra. It can be hoped that more, and more sensitive, multi-wavelength campaigns yield better arguments to evaluate and distinguish between the different jet models.

Appendix

List of observations

Table I: Not detected sources

Source	Observation ID	in added spectra #
PKS 0736−770	00039141001	–
	00039141002	–
PKS 1257−326	00038442001	–
PMN J1347−3750	00039176001	–
PMN J1603−4904	00039227001	–
PKS 2027−308	00039456001	–
	00039456002	–

Table II: Weak sources

Source	Observation ID	in added spectra #
PMN J0718−4319	00038457001	–
	00038457002	–
	00038457003	–
	00038457004	–
PKS 1144−379	00036767001	–
PKS 1424−418	00035039001	1
	00035039002	1
	00035039004	–
PKS 1454−354	00036799001	–
	00036799003	–
PMN J1802−3940	00038106001	–
	00090196001	–
PKS 1954−388	00036772001	–
	00036772003	–
	00036772004	–
PMN J2139−4235	00038411002	–
PKS 2355−534	00035049001	–
	00035049003	–

Table III: Strong sources

Source	Observation ID	in added spectra #
PMN J0810−7530	00038459001	1
	00038459002	1
	00038459003	1
	00038459004	2
	00038459005	2
	00038459006	2
PKS 1057−797	00036766001	–
	00036766002	1
	00036766003	1
PKS 1313−333	00035037003	–
PKS 1322−428	00031312002	–
	00050950002	–
	00050950004	1
	00050950005	1
	00050950006	2
	00050950007	2
	00050950008	2
	00050950009	2
PMNJ 1326−5256	00031458001	1
	00031458002	1
	00090192001	–
	00090192002	–
PKS 1333−336	00035068001	–
	00035068003	1
	00035068004	1
PKS 1440−389	00038434001	–
PKS 1549−790	00037037001	–
	00037037002	–
PKS 2005−489	00035026001	1
	00035026002	1
	00035026003	–
	00035026004	2
	00035026005	2
	00035026006	2
	00035026007	4
	00035026009	4
	00035026010	–

Table III: Strong sources

Source	Observation ID	in added spectra #
PKS 2052−474	00038412001	–
	00038412002	1
	00038412003	1
	00038412004	1
	00038412005	1
	00038412006	1
PKS 2149−306	00038412001	2
	00038412002	2
	00038412003	3
	00038412005	3
	00038412006	4
	00038412007	4
	00035242001	5
	00035242002	5
PKS 2155−304	00030795001	1
	00030795002	1
	00030795003	1
	00030795005	1
	00030795006	1
	00030795008	1
	00030795013	2
	00030795016	2
	00030795017	2
	00030795018	2
	00030795022	3
	00030795024	3
	00030795026	3
	00030795027	3
	00030795028	–
	00030795029	–
	00030795034	4
	00030795035	4
	00030795036	4
	00030795037	4
	00030795039	–
	00030795047	5
	00030795048	5
	00030795049	5
	00030795053	–
	00030795056	–
	00035027002	7
	00035027003	7
PKS 2204−540	00038409001	–

Bibliography

Aharonian, F., et al., 2009, ApJ, 695, L40

Antonucci, R., 1993, ARA&A, 31, 473

Basu, D., 2006, AJ, 131, 1231

Begelman, M. C., Blandford, R. D., & Rees, M. J., 1984, Rev. Mod. Phys., 56, 255

Begelman, M. C., Rees, M. J., & Sikora, M., 1994, ApJ, 429, L57

Bellamy, M. J., Tadhunter, C. N., Morganti, R., Wills, K. A., Holt, J., Taylor, M. D., & Watson, C. A., 2003, MNRAS, 344, L80

Beuchert, T., 2010, Radio Observations of PKS 2155-304 with the 100-m Effelsberg radio telescope, Bachelor's thesis, FAU Erlangen-Nürnberg

Bianchin, V., et al., 2009, A&A, 496, 423

Bignall, H., Cimo, G., Jauncey, D., Senkbeil, C., Lovell, J., & Ellingsen, S., 2008, The nature of gamma ray blazar candidate PMN J1326-5256, ArXiv e-prints, 0805.3891

Boeck, M., Kadler, M., Tosti, G., Burnett, T. H., Mueller, C., Ojha, R., & Wilms, J., 2010, The gamma-ray properties of radio-selected extragalactic jets, ArXiv e-prints, 1006.2538

Bolmont, J., Bühler, R., Jacholkowska, A., & Wagner, S., 2010, in AIP Conf. Ser., ed. J.-M. Alimi & A. Fuözfa, Vol. 1241, 528

Campana, S., Beardmore, A. P., Cusumano, G., & Godet, O., 2009, SWIFT-XRT-CALDB-09: Response matrices and Ancillary Response Files, SWIFT XRT CALDB RELEASE NOTE

Chang, C. S., Ros, E., Kadler, M., Ojha, R., the Fermi Lat Collaboration, the Tanami Team, & the F-Gamma Team, 2010, Multiwavelength campaign of the gamma-ray flaring source PKS 2052-47, ArXiv e-prints, 1001.1563

Donato, D., Ghisellini, G., Tagliaferri, G., & Fossati, G., 2001, A&A, 375, 739

Duller, C., 2008, Einführung in die nichtparametrische Statistik mit SAS und R, (Heidelberg: Physica-Verl.)

Fossati, G., Maraschi, L., Celotti, A., Comastri, A., & Ghisellini, G., 1998, MNRAS, 299, 433

Gehrels, N., et al., 2004, ApJ, 611, 1005

Ghisellini, G., Celotti, A., Fossati, G., Maraschi, L., & Comastri, A., 1998, MNRAS, 301, 451

Hardcastle, M. J., Worrall, D. M., Kraft, R. P., Forman, W. R., Jones, C., & Murray, S. S., 2003, ApJ, 593, 169

Healey, S. E., Romani, R. W., Taylor, G. B., Sadler, E. M., Ricci, R., Murphy, T., Ulvestad, J. S., & Winn, J. N., 2007, ApJS, 171, 61

HESS Collaboration et al., 2010, A&A, 511, A52+

Holland, S. T., 2010, The *Swift* Technical Handbook, Version 7.0.1, http://heasarc.gsfc.nasa.gov/docs/swift/proposals/tech_appd/ta/ta.html

Holt, J., Tadhunter, C., Morganti, R., Bellamy, M., González Delgado, R. M., Tzioumis, A., & Inskip, K. J., 2006, MNRAS, 370, 1633

Houck, J. C., 2010, ISIS 1.0 Technical Manual

Houck, J. C., & Denicola, L. A., 2000, in Astronomical Data Analysis Software and Systems IX, ed. N. Manset, C. Veillet, & D. Crabtree, Vol. 216, 591

Jackson, C. A., Wall, J. V., Shaver, P. A., Kellermann, K. I., Hook, I. M., & Hawkins, M. R. S., 2002, A&A, 386, 97

Kalberla, P. M. W., Burton, W. B., Hartmann, D., Arnal, E. M., Bajaja, E., Morras, R., & Poppel, W. G. L., 2005, The Leiden/Argentine/Bonn (LAB) Survey of Galactic HI: Final data release of the combined LDS and IAR surveys with improved stray-radiation corrections, http://www.citebase.org/abstract?id=oai:arXiv.org:astro-ph/0504140

Kaufmann, S., et al., 2010, in BAAS, Vol. 41, 709

Keel, B., 2002, Optical spectra of various kinds of active galactic nuclei, http://www.astr.ua.edu/keel/agn/spectra.html

Krauß, F., 2010, Swift Observations of TANAMI Counterparts, Bachelor's thesis, FAU Erlangen-Nürnberg

Krolik, J. H., 1999, Active galactic nuclei: from the central black hole to the galactic environment, Princeton University Press)

Lister, M. L., et al., 2009, AJ, 137, 3718

Marscher, A. P., 2009, Jets in Active Galactic Nuclei, ArXiv e-prints, 0909.2576

NASA, 2010, NASA missions: *Swift*, http://www.nasa.gov/mission_pages/swift/

NASA/GSFC, 2010, http://heasarc.nasa.gov/docs/swift/swiftsc.html

Nolan, P. L., et al., 1996, ApJ, 459, 100

Nowak, M. A., 2009, X-Ray spectroscopy: In theory and practice

Ojha, R., et al., 2010a, A&A, 519, A45+

Ojha, R., Kadler, M., Boeck, M., Hungwe, F., Mueller, C., Wilms, J., Ros, E., & the TANAMI Team 2010b, The TANAMI Program, ArXiv e-prints, 1006.2097

Peterson, B. M., 1997, An Introduction to Active Galactic Nuclei, Cambridge University Press)

Predehl, P., & Schmitt, J. H. M. M., 1995, A&A, 293, 889

Rieger, F. M., & Volpe, F., 2010, Short-term VHE variability in blazars: PKS 2155-304, ArXiv e-prints, 1007.4879

Sbarufatti, B., Ciprini, S., Kotilainen, J., Decarli, R., Treves, A., Veronesi, A., & Falomo, R., 2009, AJ, 137, 337

Siebert, J., Brinkmann, W., Drinkwater, M. J., Yuan, W., Francis, P. J., Peterson, B. A., & Webster, R. L., 1998, MNRAS, 301, 261

Sikora, M., Begelman, M. C., & Rees, M. J., 1994, ApJ, 421, 153

Soldi, S., et al., 2008, A&A, 486, 411

Tadhunter, C., Wills, K., Morganti, R., Oosterloo, T., & Dickson, R., 2001, MNRAS, 327, 227

Urry, C. M., & Padovani, P., 1995, PASP, 107, 803

Wilms, J., & Kadler, M., 2010, Active Galactic Nuclei, Lecture ST 2010 University Erlangen-Nürnberg, http://pulsar.sternwarte.uni-erlangen.de/wilms/teach/agn_10/

Acknowledgements

I would like to extend thanks to everyone who supported me during the time of this thesis. Special thanks go to

- M. Kadler and J. Wilms for much help and support.
- F. Krauß for help and support at any occasion at all times.
- all the "“Remeisen"” at the Dr. Remeis observatory in Bamberg, especially to L. Barragán for the help with the data extraction, M. Hanke and M. Böck for great support with the SED in particular and ISIS in general, as well as T. Beuchert.
- C. Stegmann for helpful discussion and support with the questions concerning statistics.
- B. Falkner and Ph. Hofmann for encouraging discussions and moral support.
- S. Müller and K. Müller for their perceptive critique of the manuscript.

This research has made use of the NASA/IPAC Extragalactic Database (NED) which is operated by the Jet Propulsion Laboratory, California Institute of Technology, under contract with the National Aeronautics and Space Administration, as well as the SIMBAD database, operated at CDS, Strasbourg, France.

Erklärung

Hiermit bestätige ich, dass ich diese Arbeit selbstständig und nur unter Verwendung der angegebenen Hilfsmittel angefertigt habe.

Erlangen, 21.09.2010

Martina W. Müller